

# Strong decoupling between magnetic subsystems in the low-dimensional spin- $\frac{1}{2}$ antiferromagnet $\text{SeCuO}_3$

Nikolina Novosel,<sup>1</sup> William Lafargue-Dit-Hauret,<sup>2</sup> Željko Rapljenović,<sup>1</sup> Martina Dragičević,<sup>1</sup> Helmuth Berger,<sup>3</sup> Dominik Cinčić,<sup>4</sup> Xavier Rocquefelte,<sup>2,\*</sup> and Mirta Herak<sup>1,†</sup>

<sup>1</sup>*Institute of Physics, Bijenička c. 46, HR-10000 Zagreb, Croatia*

<sup>2</sup>*Institut des Sciences Chimiques de Rennes UMR 6226, Université de Rennes 1, Campus de Beaulieu, 35042 Rennes, France*

<sup>3</sup>*Institut de Physique de la Matière Complexe, EPFL, CH-1015 Lausanne, Switzerland*

<sup>4</sup>*Department of Chemistry, Faculty of Science, University of Zagreb, Horvatovac 102A, HR-10000 Zagreb, Croatia*



(Received 4 June 2018; revised manuscript received 3 October 2018; published 28 January 2019)

The search for and understanding of low-dimensional magnetic materials is essential for both fundamental and technological purposes. Here we propose a combined experimental and theoretical investigation of such a system, namely the monoclinic phase of  $\text{SeCuO}_3$ . This low-dimensional spin- $\frac{1}{2}$  antiferromagnet appears to be based on two decoupled magnetic subsystems which respond differently to applied magnetic field in the antiferromagnetic phase. From our results we are able to propose a zero-field magnetic structure as well as a more exotic finite magnetic field structure, to be tested by future experiments. This finding is based on torque magnetometry measurements on the one side, and the use of a refined phenomenological model and state-of-the-art density functional theory calculations on the other. The existence of such systems opens a way to very exciting physics with the possibility to control separately two magnetic subsystems in one material.

DOI: [10.1103/PhysRevB.99.014434](https://doi.org/10.1103/PhysRevB.99.014434)

## I. INTRODUCTION

Low-dimensional spin systems represent a fertile ground to study the influence of quantum effects on the formation of exotic states of matter [1]. Zero-dimensional (0D) systems, in particular, are of significance since simple finite lattices represent an interesting playground for theoretical investigations, while at the same time, 0D magnetic lattices can be found in real materials allowing the theory to be tested.

The simplest example of a 0D system is a spin dimer consisting of two spins coupled by the exchange energy  $J$ . The two allowed states are singlet and triplet separated by an energy gap  $J$  and the ground state is determined by the sign of  $J$  (antiferromagnetic or ferromagnetic coupling). In real materials small but finite interactions between the 0D units result in cooperative behavior and most often lead to a long-range magnetic ordering. Magnetic order combined with the quantum effects of underlying 0D magnetic units results in exotic phase diagrams where different phases can be obtained by tuning the relative strength of the exchange couplings. A well studied example with a rich phase diagram is the Shastry-Sutherland model consisting of orthogonal dimers coupled by frustrated interdimer interaction [2]. Both spin singlets and long-range antiferromagnetic order can be found as ground states, depending on the ratio between intradimer and interdimer interaction [3].

Another example of a 0D system is a spin tetramer where four spins  $S_a$ ,  $S_b$ ,  $S_c$ , and  $S_d$  interact forming a 0D magnetic

unit with a slightly more complex excitation spectrum than found in a spin dimer [4]. When the coupling between spins  $S_a$  and  $S_b$  is equal to the coupling between spins  $S_c$  and  $S_d$ , the spin Hamiltonian can be written as

$$\mathcal{H} = J_{12} (\mathbf{S}_a \cdot \mathbf{S}_b + \mathbf{S}_c \cdot \mathbf{S}_d) + J_{11} (\mathbf{S}_b \cdot \mathbf{S}_c). \quad (1)$$

An interesting limit for the spin tetramer occurs when the coupling  $J_{11}$  between the two spins in the middle,  $S_b$  and  $S_c$ , is antiferromagnetic (AFM) and much stronger than the coupling  $J_{12}$  of spins in the middle,  $S_b$  and  $S_c$ , with spins on the sides of the tetramer,  $S_a$  and  $S_d$  (see Fig. 1). In this case  $S_b$  and  $S_c$  are expected to form a singlet state which persists in the background of weakly connected paramagnetic spins  $S_a$  and  $S_d$ . At low temperatures weak intertetramer interactions can lead to a long-range magnetic order. When this happens, the question arises as to whether singlet states are broken or whether they persist as singlets in the background of long-range magnetically ordered spins  $S_a$  and  $S_d$ . The latter scenario was proposed by Hase *et al.* for the spin tetramer system  $\text{CdCu}_2(\text{BO}_3)_2$ , based on high-field magnetization measurements [5], and it was recently confirmed by nuclear magnetic resonance (NMR) and zero-field muon spin relaxation (ZF- $\mu$ SR) [6]. This opens up a possibility to study new types of quantum spin systems where exotic behavior may be tuned by the ratio of intratetramer and intertetramer interactions. In order to better understand how this type of ordering emerges it is important to find and study new systems which might host such exotic behavior.  $\text{SeCuO}_3$ , studied in this work, is in many aspects similar to  $\text{CdCu}_2(\text{BO}_3)_2$  and thus represents an ideal candidate to study selective spin correlations [7], especially since, unlike for the latter, high-quality single crystals are available.

\*xavier.rocquefelte@univ-rennes1.fr

†mirta@ifs.hr

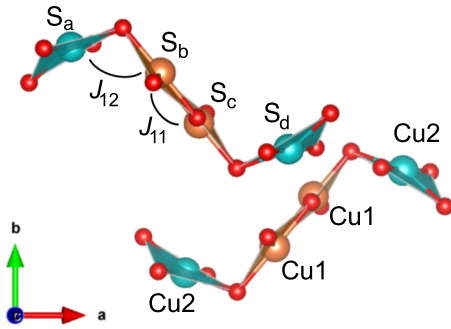


FIG. 1. Two magnetically inequivalent tetramers in  $\text{SeCuO}_3$  as proposed in Ref. [7]. Cu1 atoms are shown in orange color, Cu2 in blue, and O atoms in red. Se atoms are not shown for simplicity.

$\text{SeCuO}_3$  crystals belong to the monoclinic space group  $P2_1/n$  with unit cell parameters  $a = 7.712 \text{ \AA}$ ,  $b = 8.238 \text{ \AA}$ ,  $c = 8.498 \text{ \AA}$ , and  $\beta = 99.124^\circ$  [8]. Two crystallographically inequivalent copper sites, Cu1 and Cu2, are present in the monoclinic phase of  $\text{SeCuO}_3$ , each surrounded by six oxygen ligands forming a Jahn-Teller distorted elongated  $\text{CuO}_6$  octahedron [8]. This ligand configuration suggests a  $d_{x^2-y^2}$  orbital state for the unpaired copper spin  $S = \frac{1}{2}$ . Taking into account the local environment of the magnetic ion  $\text{Cu}^{2+}$ , it was proposed in Ref. [7] that quasi-isolated linear spin tetramers  $\text{Cu2-Cu1-Cu1-Cu2}$  are present in  $\text{SeCuO}_3$  (see Fig. 1). The temperature dependence of the magnetic susceptibility, however, does not seem to support the simple tetramer model [7,9,10]. The temperature dependence of the electron  $\mathbf{g}$  tensor accompanied by the rotation of the macroscopic magnetic axes in a paramagnetic state [7,10] was attributed to site-selective spin correlations. The nuclear spin-spin relaxation rate  $1/T_2$  obtained from NMR unveiled the development of site-specific spin correlations [11]. A recent nuclear quadrupole resonance (NQR) study proposed that Cu1 spins are strongly coupled forming a spin singlet state at temperatures  $T < J_{11} \approx 200 \text{ K}$  [12].

Below  $T_N = 8 \text{ K}$ ,  $\text{SeCuO}_3$  exhibits a long-range AFM order [7,10–12]. Temperature dependence of the magnetic susceptibility anisotropy below  $T_N$ , in low magnetic field, is typical for uniaxial antiferromagnets [7,10]. A spin-flop transition is observed around  $H_{\text{SF}} \approx 1.8 \text{ T}$  at  $T = 2 \text{ K}$  when the magnetic field is applied along the easy axis [7]. The high-field magnetization measurements show the existence of a half-step magnetization plateau [11], similar to what was found in the previously mentioned  $\text{CdCu}_2(\text{BO}_3)_2$  compound where the plateau emerges from the polarization of weakly coupled Cu2 spins while Cu1 dimers remain in the singlet state [5]. The  $^{77}\text{Se}$  NMR measurements reveal a different temperature dependence of the Cu1 and Cu2 spin-spin relaxation rate  $1/T_2$  in the AFM state of  $\text{SeCuO}_3$  which could be the signature of two subsystems, one consisting of strongly coupled Cu1 dimers and another of weakly coupled Cu2 spins [11]. The difference of Cu1 and Cu2 magnetic sites is also observed in neutron powder diffraction measurements which give  $m_{\text{Cu1}} \approx 0.35 \mu_B$  and  $m_{\text{Cu2}} < 0.8 \mu_B$  at  $1.5 \text{ K}$  with a smaller value for the Cu1 site confirmed by NQR [12]. Magnetic structure from neutron powder diffraction was

found to be noncollinear [12]. All these observations confirm that  $\text{SeCuO}_3$  has an unconventional AFM ground state and thus represents an ideal new host to study exotic magnetic behavior influenced by quantum phenomena.

In this work we experimentally probe the magnetic anisotropy of the AFM state in  $\text{SeCuO}_3$  using torque magnetometry measurements in magnetic fields  $H \lesssim 5 \text{ T}$  which are significantly higher than the spin-flop field  $H_{\text{SF}} \approx 1.8 \text{ T}$ . This allows us to determine the magnetocrystalline anisotropy energy (MAE) of  $\text{SeCuO}_3$  as well as to observe field-induced spin reorientation. We complete the description of the MAE by a theoretical investigation based on first-principles calculations.

This paper is organized as follows. In Secs. II A and II B we give a brief overview of the experimental and theoretical methods used in this work. In Sec. III A the results of torque measurements are presented. An analysis of the torque data using a phenomenological model is presented in Sec. III B, and the density functional theory results are given in Sec. III C. The obtained experimental and theoretical results are discussed in Sec. IV. Finally, Sec. V is dedicated to concluding remarks.

## II. METHODS

### A. Experimental

Single crystals of monoclinic  $\text{SeCuO}_3$  have been grown by a standard chemical vapor phase method, as described in the literature [7].

The magnetic torque was measured by a home-built calibrated torque apparatus based on the torsion of a thin quartz fiber. The magnetic field was supplied by a Cryogenic Consultants 5 T split-coil superconducting magnet with a room-temperature bore. The quartz sample holder is placed in a separate cryostat which is mounted in the room-temperature bore of a magnet cryostat. The monitoring and control of the sample temperature were performed using a Lakeshore 336 temperature controller. For magnetic torque measurements a single crystal of mass  $(246 \pm 8) \mu\text{g}$  was used with the  $b$  axis parallel to the longest crystal axis and with the two crystal planes,  $(1\ 0\ 1)$  and  $(1\ 0\ \bar{1})$ , easily distinguishable.

### B. Theory

The present calculations are based on the spin-polarized density functional theory as implemented in the WIEN2k package [13] using a full potential linear augmented plane wave method. The Perdew-Burke-Ernzerhof approximation (PBE) [14] is considered for the exchange and correlation part. A Hubbard effective term within the Anisimov approach [15] was used to describe the Cu  $3d$  orbitals more properly, allowing us to obtain magnetic moments for the copper sites close to  $0.73 \mu_B$ . We also checked our calculations considering the on-site PBE0 hybrid functional [16], giving similar results. The  $R_{\text{MT}}$  muffin-tin radii for Se, Cu, and O atoms were set to 1.65, 1.96, and 1.49 bohrs and the  $RK_{\text{max}}$  to 6. The separation between valence and core states was set to  $-6 \text{ Ry}$ , except for the calculations including zinc atoms (set to  $-8 \text{ Ry}$ , with  $R_{\text{MT}} = 1.96$  bohrs). The Brillouin zone sampling was done using a  $5 \times 4 \times 4$   $k$  mesh [17].

### III. RESULTS

#### A. Experimental results

For a simple collinear uniaxial antiferromagnet in low magnetic field  $H \ll H_{\text{SF}}$ , the magnetization is linearly dependent on the magnetic field. Consequently, the angular dependence of the measured component of magnetic torque  $\tau_z$  is then described by the expression

$$\tau_z = \tau_0 \sin(2\varphi - 2\varphi_0), \quad (2)$$

where amplitude  $\tau_0$  is given by

$$\tau_0 = \frac{m}{2M_{\text{mol}}} \Delta\chi_{xy} H^2. \quad (3)$$

$m$  is the mass of the sample,  $M_{\text{mol}}$  is the molar mass, and  $H$  is the magnitude of the applied magnetic field.  $\Delta\chi_{xy} = \chi_x - \chi_y$  is the magnetic susceptibility anisotropy in the  $xy$  plane in which the magnetic field rotates.  $x$  and  $y$  are, respectively, the directions of the maximal and minimal susceptibility components in the plane of measurement.  $\varphi$  is the goniometer angle and  $\varphi_0$  is the angle at which the field is parallel to  $x$ . Equations (2) and (3) show that, in the case of a linear response, the magnetic torque is proportional to  $H^2$  and  $\Delta\chi$  and the angular dependence of the torque is a sine curve with a period of  $180^\circ$ . The previously published low-field ( $H \lesssim 0.2$  T) torque data [10] in both paramagnetic and antiferromagnetic states are well described by Eqs. (2) and (3).

The magnetic torque was measured in the AFM state at  $T = 4.2$  K by rotating the magnetic field in three crystal planes: the  $ac$  plane, the plane spanned by the  $b$  and  $[\bar{1} 0 1]^*$  axes, and the plane spanned by the  $b$  and  $[1 0 1]^*$  axes. The angular dependence of the torque for these three planes is shown in Fig. 2. It can be readily observed that the measured torques for the  $ac$  plane and the plane spanned by the  $b$  and  $[\bar{1} 0 1]^*$  axes [Figs. 2(a) and 2(c), respectively] are not regular sine curves and cannot be described by Eq. (2). The deviation of the torque curves from Eq. (2) is the most pronounced in the  $ac$  plane for  $H = 2$  T, which is close to the spin-flop field  $H_{\text{SF}} \approx 1.8$  T [7]; see Fig. 2(a). Moreover, the amplitude of torque for these two planes does not increase linearly with  $H^2$ , which is shown for the  $ac$  plane in Fig. 2(b). The low-field behavior is well represented by the dashed line with the slope given by  $(m/2)M_{\text{mol}}\Delta\chi_{xy}$  [see Eq. (3)] with  $\Delta\chi$  obtained from the low-field measurements [10]. The deviation from the low-field behavior is observed already for  $H \gtrsim 1.5$  T. The  $H^2$  dependence is restored for  $H \geq 2$  T, but with a much smaller slope which, according to Eq. (3), corresponds to a weaker susceptibility anisotropy  $\Delta\chi$ . Finally, Fig. 2(d) shows the torque data multiplied by  $2M_{\text{mol}}/(mH^2)$  for the plane spanned by the  $b$  and  $[1 0 1]^*$  axes. For this plane, all the curves are superimposed upon one another, as predicted by Eqs. (2) and (3).

The observed deviation of the torque curves from Eq. (2) is a signature of the spin reorientation (i.e., reorientation of the Néel vector) which appears when the applied magnetic field is comparable to or greater than the spin-flop field  $H_{\text{SF}}$ . In the plane spanned by the  $b$  and  $[1 0 1]^*$  axes [see Fig. 2(d)] measured curves follow Eq. (2), so we can conclude that the reorientation seems to be confined to the  $ac$  plane and the plane spanned by the  $b$  and  $[\bar{1} 0 1]^*$  axes. The spin

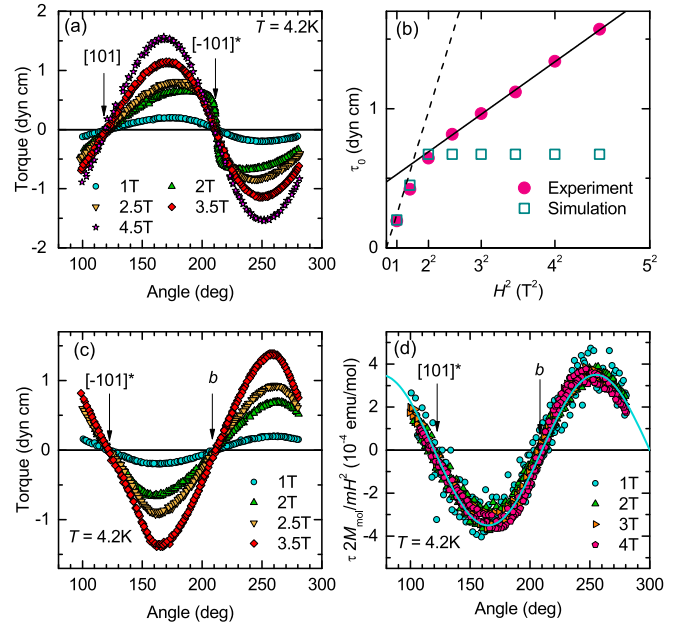


FIG. 2. Angular dependence of torque  $\tau$  measured in three crystal planes in different magnetic fields. (a) The torque measured in the  $ac$  plane. (b) Full symbols: The dependence of torque amplitude  $\tau_0$  on  $H^2$  in the  $ac$  plane [see (a)]. Solid line is fit to the experimental data for  $H > H_{\text{SF}}$ . Dashed line represents expected  $H^2$  dependence of the torque amplitude for an antiferromagnet with no reorientation (extrapolation of  $H \ll H_{\text{SF}}$  data using Eq. (3) and low-field anisotropy data [10]). Empty symbols represent simulation (see Sec. III B). (c) Angular dependence of torque measured in the plane spanned by  $b$  and  $[\bar{1} 0 1]^*$  axes, and (d) the plane spanned by  $b$  and  $[1 0 1]^*$  axes. In (d) the torque is multiplied by  $2M_{\text{mol}}/(mH^2)$  resulting in practically the same curve for all applied fields. This is consistent with no reorientation of spins in this plane [see Eq. (2)]. The angles corresponding to the specific crystal directions are pointed by arrows.

reorientation in the antiferromagnet can be easily simulated using phenomenological magnetocrystalline anisotropy energy, as we will show in Sec. III B. However, this simple model cannot reproduce the finite slope of the torque amplitude observed in Fig. 2(d) but rather predicts a field-independent amplitude [open squares in Fig. 2(d)]. We will show that in order to reproduce the measured curves, it is necessary to assume two decoupled subsystems and a site-specific spin reorientation in  $\text{SeCuO}_3$ , which is the main result of our work.

#### B. Phenomenological model of spin reorientation in $\text{SeCuO}_3$

The spin reorientation in a collinear antiferromagnet in a finite applied magnetic field was first proposed by Néel in 1936 [18,19], who observed that the competition between the orientation of spins, defined by the magnetocrystalline anisotropy energy (MAE), and the orientation preferred by the Zeeman energy results in a reorientation of spins, i.e., the Néel vector which minimizes the total energy.

The MAE determines the spin orientation in the absence of a magnetic field (easy axis direction), while Zeeman energy for an antiferromagnet is minimal when spins are

perpendicular to the applied magnetic field. Depending on the magnitude and direction of the applied field, spins will be oriented in such a way to minimize the total energy while still maintaining an almost collinear AFM structure since the superexchange energy is much larger than the anisotropy energy. When magnetic field is applied along the easy axis, the spins reorient perpendicularly to the magnetic field when the field reaches a critical value  $H_{SF}$ , called the *spin-flop* field. The magnitude of the spin-flop field depends on the magnitude of the MAE, as well as the magnetic susceptibility anisotropy [20]. Spin-flop transitions were observed in many antiferromagnets and studied in detail in the literature (see, e.g., Ref. [21] and references therein).

A simple phenomenological approach can be used to study field-induced spin reorientation in antiferromagnets with different symmetries. Specifically, torque magnetometry measurements can be employed to determine the MAE shape and also to study the spin axis reorientation in a finite magnetic field for uniaxial antiferromagnets [22], as well as antiferromagnets with higher symmetries and multiple antiferromagnetic domains [23,24]. The same approach is used in this work to determine the MAE shape and the spin reorientation in finite magnetic fields in the AFM state of  $\text{SeCuO}_3$ .

The total phenomenological energy  $\mathcal{F}_{\text{tot}}$  of the sample in a finite magnetic field is the sum of MAE  $\mathcal{F}_a(\theta, \phi)$  and Zeeman term  $\mathcal{F}_Z(\psi, \xi, \theta, \phi)$ :

$$\mathcal{F}_{\text{tot}}(\theta, \phi, \psi, \xi) = \mathcal{F}_a(\theta, \phi) + \mathcal{F}_Z(\psi, \xi, \theta, \phi). \quad (4)$$

In the following we use the coordinate system spanned by the magnetic eigenaxes in the AFM state below  $\approx 6$  K, ( $[\bar{1}01]^*$ ,  $[101]$ ,  $b$ ), determined previously [10] and confirmed in this work. Coordinates  $\theta$  and  $\psi$  represent polar and  $\phi$  and  $\xi$  azimuthal angles in a spherical coordinate system defined with respect to the ( $[\bar{1}01]^*$ ,  $[101]$ ,  $b$ ) coordinate system. The simplest expression for MAE in the chosen coordinate system is [25]

$$\mathcal{F}_a(\theta, \phi) = K_0 + K_1 \sin^2 \theta \sin^2 \phi + K_2 [(1 + \cos^2 \phi) \sin^2 \theta - 1], \quad (5)$$

where  $\theta$  and  $\phi$  are the polar and azimuthal angles (see Fig. 3), and  $K_1$  and  $K_2$  are the anisotropy constants expressed in units of erg/mol. Second-order terms to the anisotropy energy  $\mathcal{F}_a$ , written in Eq. (5), are sufficient to study the reorientation of the spin axis in a finite magnetic field, as long as we do not try to describe the critical behavior in magnetic fields very close to  $H_{SF}$  [21].

Equation (5) describes the amount of energy needed to rotate the spin axis away from the easy axis direction. Depending on the value and sign of the anisotropy constants  $K_1$  and  $K_2$ , the anisotropy energy (5) can have several different shapes allowed by symmetry. Our previous as well as current results show that the  $b$  axis is the hard axis, while  $[\bar{1}01]^*$  and  $[101]$  are the easy and intermediate axes, respectively. This puts the following constraints on the MAE (5) constants:  $K_2 < 0$  and  $K_2 < K_1$ . The resulting experimental MAE found in this work is shown in Fig. 3.

The Zeeman energy in Eq. (4) is given by

$$\mathcal{F}_Z(\psi, \xi) = -\frac{1}{2} \mathbf{H}(\psi, \xi) \cdot \hat{\chi} \cdot \mathbf{H}(\psi, \xi), \quad (6)$$

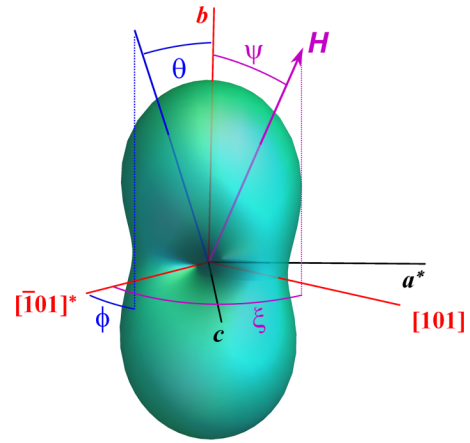


FIG. 3. The MAE shape in  $\text{SeCuO}_3$  obtained from the torque measurements in this work. Red lines represent the magnetic axes which are also extrema of the anisotropy energy. Easy axis direction (a global minimum) is along the  $[\bar{1}01]^*$  axis. Polar and azimuthal angles  $\theta$  and  $\phi$  used in the spherical coordinate system throughout the paper are also shown, as well as the  $\psi$  and  $\xi$  defining the direction of magnetic field  $\mathbf{H}$ .

where  $\mathbf{H}(\psi, \xi)$  is the applied magnetic field and here  $\hat{\chi}$  is the magnetic susceptibility tensor of the sample expressed in the same coordinate system as the MAE (5).  $\psi$  and  $\xi$  are polar and azimuthal angles representing the direction of the magnetic field  $\mathbf{H} = H(\cos \xi \sin \psi, \sin \xi \sin \psi, \cos \psi)$  and are defined as shown in Fig. 3.

In zero and very low magnetic fields the susceptibility tensor  $\hat{\chi}$  in the chosen coordinate system spanned by magnetic eigenaxes is given by

$$\hat{\chi}_0 = \begin{bmatrix} \chi_{[\bar{1}01]^*} & 0 & 0 \\ 0 & \chi_{[101]} & 0 \\ 0 & 0 & \chi_b \end{bmatrix}. \quad (7)$$

In finite magnetic field, the spin axis, i.e., the Néel vector, will in general start to rotate away from the direction of the easy axis in order to minimize the total energy (4). We describe this rotation by allowing the susceptibility tensor to rotate:

$$\hat{\chi}(\theta, \phi) = \mathbf{R}(\theta, \phi) \cdot \hat{\chi}_0 \cdot \mathbf{R}^T(\theta, \phi), \quad (8)$$

where  $\hat{\chi}_0$  is the low-field ( $H \ll H_{SF}$ ) susceptibility tensor given by expression (7) and  $\mathbf{R}(\theta, \phi)$  is the rotation matrix. Our torque measurements were performed at  $T = 4.2$  K where  $\chi_{[\bar{1}01]^*} = 4 \times 10^{-4}$  emu/mol,  $\chi_{[101]} = 3.5 \times 10^{-3}$  emu/mol, and  $\chi_b = 3.8 \times 10^{-3}$  emu/mol [7,10].

Having defined all the ingredients of the total energy (4), we can proceed to simulate our experimental results. For an anisotropic antiferromagnetic sample placed in finite magnetic field  $\mathbf{H}(\psi, \xi)$ , the new direction of the spin axis, i.e., the Néel vector, is obtained numerically by minimizing the total energy  $\mathcal{F}_{\text{tot}}$  with respect to  $\theta$  and  $\phi$ . To simulate the experimental results we start by finding  $K_1$  and  $K_2$  values which satisfy the above mentioned requirements for the MAE extrema. A correct choice of values must reproduce the experimental  $H_{SF}$  value of approximately 1.8 T at  $T = 2$  K when the magnetic field is applied along the easy axis. In the present case, the spin-flop field is given by

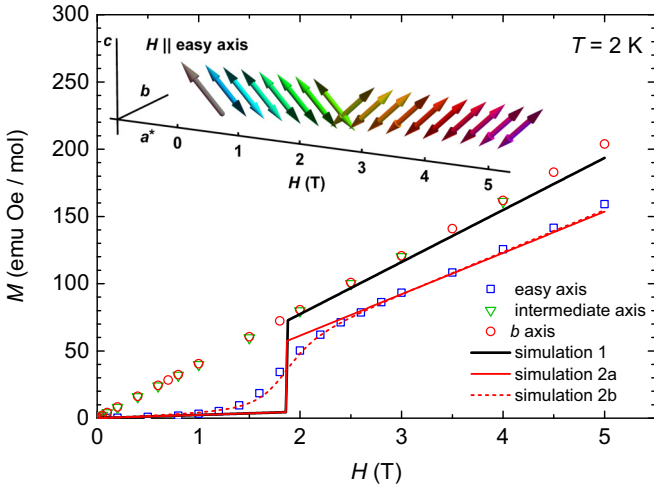


FIG. 4. A simulation of the magnetization dependence on magnetic field when  $H$  is parallel to the easy axis compared to the experimental result at  $T = 2$  K published in Ref. [7] (empty blue squares). Inset: The dependence of the spin axis direction on applied magnetic field obtained from simulation. Simulation 1 allows all spins to rotate simultaneously. Simulation 2 allows only a fraction of the spins to rotate, as described in the main text. Solid red line (2a) represents the result for  $H \parallel$  easy axis, while dashed line (2b) simulates a misorientation of the sample by  $10^\circ$ , to mimic probable misorientation in our experiment.

$H_{\text{SF}} = [2(K_1 - K_2)/(\chi_{[101]} - \chi_{[\bar{1}01]^*})]^{1/2}$  [21,26]. The choice which gives  $K_2 - K_1 = -6.35 \times 10^5$  erg/mol gives  $H_{\text{SF}} = 1.87$  T for values of the susceptibility tensor measured at  $T = 2$  K [10], well within the experimental margin of error.

Next we proceed by applying magnetic field  $\mathbf{H}(\psi_0, \xi_0)$  in the direction defined by  $(\psi_0, \xi_0)$  and find the values of  $(\theta_0, \phi_0)$  which minimize the total energy (4). This allows us to calculate a rotated susceptibility tensor (8) and finally the magnetization from  $\mathbf{M} = \hat{\chi}(\theta_0, \phi_0) \cdot \mathbf{H}(\psi_0, \xi_0)$ .

To test our approach we first simulate the experimental magnetization curve for field applied along the easy axis direction. The resulting curve (simulation 1), shown by the solid black line in Fig. 4, is compared to the measured values from Ref. [7] represented by empty blue squares in Fig. 4. The spin-flop transition is clearly observed at  $H_{\text{SF}} = 1.87$  T in the calculated curve. From our simulation we obtain the accompanying direction of the spin axis, i.e., the Néel vector which is shown in the inset of Fig. 4. The spins flop from the easy axis direction for  $H < H_{\text{SF}}$  to the intermediate axis direction  $H > H_{\text{SF}}$ . However, for  $H > H_{\text{SF}}$ , the calculated magnetization values (solid black line in Fig. 4) are somewhat larger than the measured ones (empty blue squares) and in fact fall on values obtained for magnetization measured along the intermediate and the hard axes (empty green triangles and red circles in Fig. 4). This points to the anomalous behavior of spin reorientation in  $\text{SeCuO}_3$ , a point to which we will return.

Next, we simulate the measured torque curves in a similar manner, by rotating the magnetic field, as in experiment, while repeating the minimization procedure. The torque is calculated from the obtained magnetization and applied field for each value and direction of magnetic field using  $\tau =$

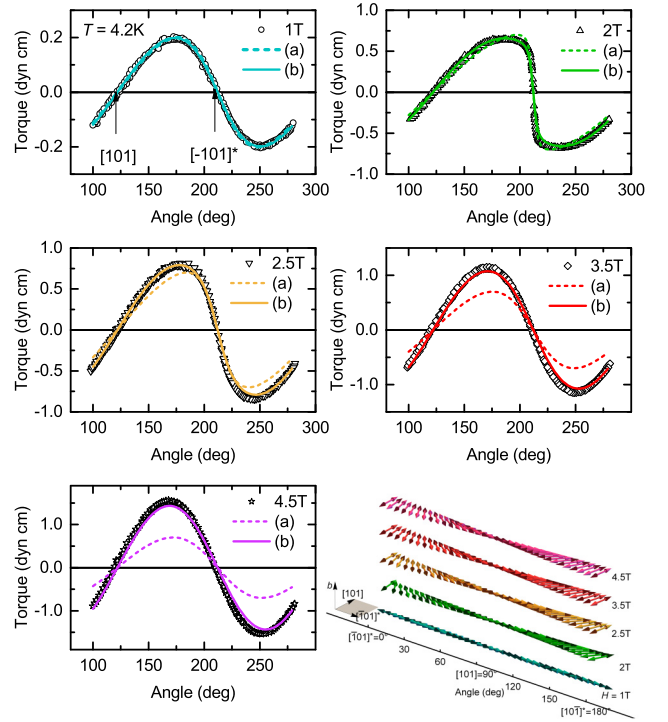


FIG. 5. The torque measured in the  $ac$  plane in different magnetic fields compared to two different simulations, as described in the main text. (a) A simulation with reorientation of all spins. (b) A simulation allowing the site-specific reorientation. Bottom right panel: The angle-dependent reorientation of the spin axis obtained from the simulation shown in the laboratory coordinate system. Double-headed arrow represents the direction of the spin axis, i.e., the Néel vector. In the case of partial spin reorientation (see text) the plotted arrows correspond to subsystem 2 while for subsystem 1 the spin axis remains in the easy axis direction. The plane of rotation of the magnetic field is shown as a dark square in the accompanying coordinate system. The angle is measured with respect to the  $[\bar{1}01]^*$  axis, while in other panels a goniometer angle is shown.

$(m/M_{\text{mol}})\mathbf{M} \times \mathbf{H}$ , where  $m$  is the mass and  $M_{\text{mol}}$  the molar mass of the sample. The torque experiment was performed at 4.2 K. The experimental value of  $H_{\text{SF}}$  is the same at  $T = 4.2$  K as at 2 K, within the experimental uncertainty [7]. Since the susceptibility tensor components are slightly different at 4.2 K, we need to take  $K_1 - K_2 = 5.42 \times 10^5$  erg/mol in order to reproduce  $H_{\text{SF}} \approx 1.87$  T at  $T = 4.2$  K.

The angular dependence of the torque in the  $ac$  plane obtained by simulation is compared to experimental results in Fig. 5. The simulations agree very well with the measurements for  $H \leq 2$  T. However, at higher magnetic fields the calculated curves have smaller amplitude than the experimental curves, and the discrepancy increases as the field increases. One possible reason for the observed discrepancy could be lowering of the symmetry which would allow a different MAE shape. This, however, is not supported by our experiment (see tensor (7) in agreement with symmetry requirements [27]) nor by neutron diffraction experiment [12]. Large misorientation of the sample could account for the observed deviations; however it was not realized in experiment.

In Fig. 2(b) we already compared the experimental and calculated results for torque amplitude. Independence of the torque amplitude from magnetic field for  $H \geq H_{SF}$ , obtained from our calculation, is also observed in the torque experiment for conventional spin reorientation in uniaxial collinear antiferromagnets [26,28] and is in agreement with the results of Néel [18,19]. In our experiment  $\tau_0 \propto H^2$  both in low magnetic field and for  $H \geq 2$  T [see Fig. 2(b)], but the slope is much smaller in higher field. This can be interpreted as if only a fraction of spins reorient in applied magnetic field, while the rest continue to exhibit the low-field behavior. The slope of linear curves in Fig. 2(b) is proportional to the susceptibility anisotropy  $\Delta\chi$  in the plane of measurement [see Eq. (3)]. Taking this into account we obtain for the ratio of the high-field and low-field amplitudes  $\Delta\chi_{HF}/\Delta\chi_{LF} = 0.22$ .

Following the assumption that only part of the spins reorient in finite magnetic field we attempt to obtain a better agreement between experiment and simulation by dividing the susceptibility tensor into two parts,

$$\hat{\chi} = \hat{\chi}_1 + \hat{\chi}_2. \quad (9)$$

In experiment only the macroscopic total tensor  $\hat{\chi}$  is measured, so we make an assumption that there are two subsystems which both participate in the long-range AFM order and we construct their susceptibility tensors from  $\hat{\chi}_0$ :

$$\hat{\chi}_1 = n \hat{\chi}_0, \quad \hat{\chi}_2 = (1 - n) \hat{\chi}_0, \quad (10)$$

where  $\hat{\chi}_0$  is given by Eq. (7). Following the result of Ref. [12] which claims that the magnetic moments on different Cu sites are different, we allow different weights for  $\hat{\chi}_1$  and  $\hat{\chi}_2$ . The expression (10) is written under the assumption that both tensors share the same magnetic eigenaxes. The parameter  $n$  describes the contribution of  $\hat{\chi}_1$  to  $\hat{\chi}_0$ , i.e., the induced magnetization of subsystem 1 to the total induced magnetization  $\mathbf{M} = \mathbf{M}_1 + \mathbf{M}_2 = (\hat{\chi}_1 + \hat{\chi}_2) \cdot \mathbf{H}$ . The spins of subsystem 1 do not reorient in finite magnetic field, while those of subsystem 2 do, so the rotation matrix in Eq. (8) acts only on  $\hat{\chi}_2$  and  $H_{SF} = [2(K_1 - K_2)/\Delta\chi_2]^{1/2}$ , where  $\Delta\chi_2$  represents the susceptibility anisotropy of subsystem 2 [see Eq. (10)]. To reproduce  $H_{SF} = 1.87$  T at  $T = 2$  K we set  $K_1 - K_2 = 4.95 \times 10^5$  erg/mol and  $n = 0.22$ . The resulting simulated magnetization for these parameters is shown in Fig. 4 (simulation 2a). The spin-flop transition is sharp, as expected for a perfect orientation of the sample. Furthermore, our calculation now reproduces the measured magnetization values in all applied fields. Including a possible misorientation in the simulation (less than  $10^\circ$ ) we obtain the dashed red curve (simulation 2b) in Fig. 4, in perfect agreement with experiment.

Torque curves calculated using assumption (10) for separate subsystems are shown by solid lines in Fig. 5. Curves were obtained using the following set of parameters:  $K_1 = -0.6 \times 10^5$  erg/mol and  $K_2 = -4.83 \times 10^5$  erg/mol at 4.2 K [29] and  $n = 0.22$ . The value of  $n$  agrees perfectly with the ratio of high and low field susceptibility anisotropies  $\Delta\chi_{HF}/\Delta\chi_{LF}$  we obtained from analysis of torque amplitudes for  $H$  below and above the spin-flop field [see Fig. 2(b)]. The corresponding magnetocrystalline anisotropy energy is shown in Fig. 3.

In Fig. 6 we compare the torque measurements for a magnetic field rotating in the plane spanned by  $b$  and  $[\bar{1}01]^*$

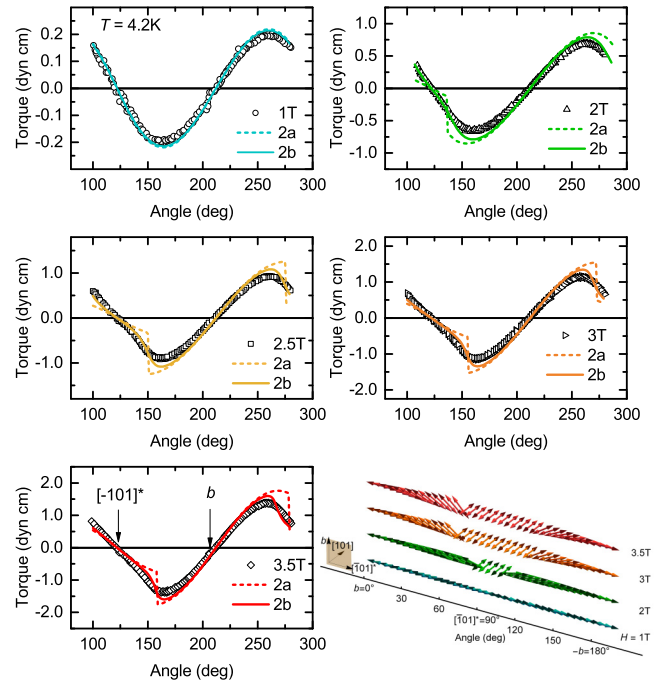


FIG. 6. The torque measured in the plane spanned by  $b$  and  $[\bar{1}01]^*$  axes compared to the results of simulation, as described in the main text. Dotted lines represent a perfect orientation (2a), and solid lines simulate a slightly misoriented sample (2b). Only site-specific simulation is shown. Bottom right panel: Angle-dependent spin axis reorientation for perfect orientation of the sample shown in the laboratory coordinate system. Double-headed arrow represents the direction of the spin axis, i.e., the Néel vector. In the case of partial spin reorientation (see text) plotted arrows correspond to subsystem 2 while for subsystem 1 the spin axis remains in the easy axis direction. The plane of rotation of the magnetic field is shown as a dark square in the accompanying coordinate system. The angle is measured with respect to the  $b$  axis, while in other panels the goniometer angle is shown.

axes with the simulation in the plane spanned by easy and hard axes. Sharp transitions are expected in the case of a perfect orientation (dashed curves) while a simulation with a small misorientation (solid lines) gives a better agreement with the experiment. In the bottom right panel of both Fig. 5 and Fig. 6 we plot the reorientation of the spin axis corresponding to the torque curves obtained from our simulation for different fields. Finally, in Fig. 7 we see an excellent agreement between experimental and simulated data for the plane spanned by the  $b$  and  $[101]^*$  axes.

### C. Magnetic properties estimated from density functional theory

In parallel with our experimental investigations of the magnetic anisotropy of  $\text{SeCuO}_3$ , we have carried out density functional theory (DFT) calculations including spin-orbit coupling (SOC), using a similar strategy to the one we considered for the low-dimensional magnetic compound  $\text{CuO}$  [30]. Indeed, we demonstrated that the estimation of the MAE of  $\text{CuO}$ , considering its antiferromagnetic ground state, allows us to properly predict its easy axis of magnetization. In contrast to

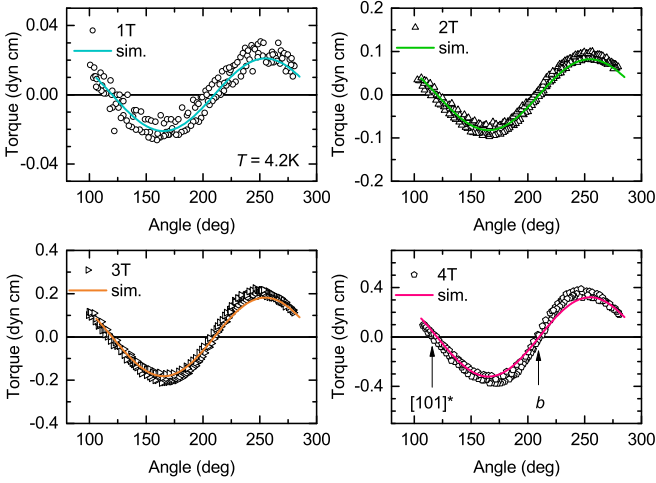


FIG. 7. The torque measured in the plane spanned by  $b$  and  $[101]^*$  axes compared to the results of the site-specific simulation (sim.), as described in the main text.

CuO, spin fluctuations seem to play a major role in  $\text{SeCuO}_3$  magnetic properties. Živković *et al.* have already pointed out the possibility to observe these quantum fluctuations in  $\text{SeCuO}_3$ , and evoked a possible difference of the magnetic moment values between the Cu1 and Cu2 sites [7]. More recently, Lee *et al.* mentioned that the site-specific spin correlation may be explained by considering two subsystems based on strongly coupled Cu1 dimers and weakly interacting Cu2 spins [11]. They conclude that such a scheme will lead to smaller ordered magnetic moments for Cu1 than for Cu2 due to singlet fluctuations. Also, the reduced ordered magnetic moment of Cu1 sites has been confirmed based on the neutron powder diffraction and NQR measurements [12]. However, none of the magnetic models proposed so far explain all the experimental measurements. It is thus essential to provide a theoretical basis to clarify the present picture.

Our previous investigation, based on magnetic susceptibility measurements, leads to the conclusion that the Cu2-Cu1-Cu1-Cu2 tetramer is based on two antiferromagnetic couplings, namely  $J_{11} = 225$  K and  $J_{12} = 160$  K [7]. The magnetic anisotropy energy (MAE) has then been estimated for the AF1 ground-state magnetic structure [shown in Fig. 8(a)],

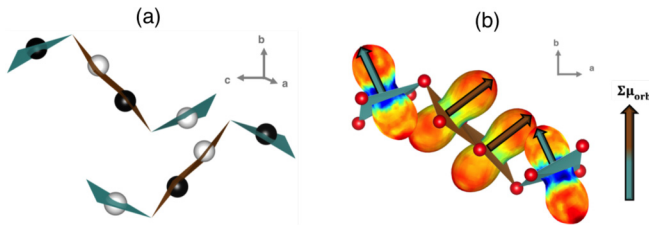


FIG. 8. (a) Antiferromagnetic order considered in our DFT calculations. The  $\text{Cu}^{2+}$  sites are depicted as filled and empty circles, representing up-spin and down-spin, respectively. (b) Orbital moment of one tetramer. Red and blue colors show the maximum and minimum of the orbital moment, respectively. The arrow on the right side shows the vector sum of orbital moments represented by brown and blue vectors on Cu1 and Cu2 sites, respectively.

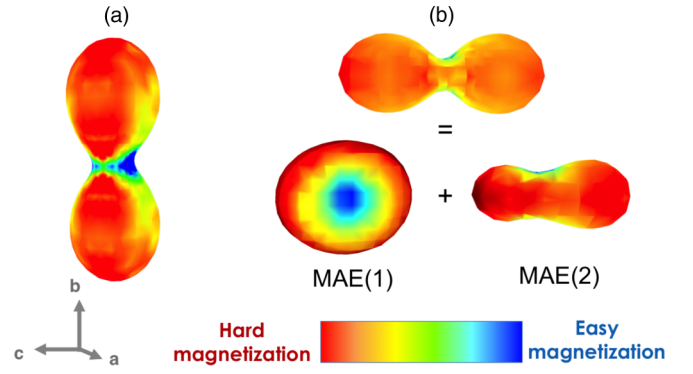


FIG. 9. (a) Experimental MAE. (b) Contributions MAE1 (MAE2) to the total MAE (top) determined substituting Cu2 (Cu1) by Zn atoms and considering a  $U_{\text{eff}} = 5$  eV correction for Cu sites.

using the code WIEN2k with the GGA+U and PBE0 hybrid functionals and including the spin-orbit coupling. MAE corresponds to an energy difference between two directions of the magnetization density. Because the present compound is monoclinic, the  $[010]$  direction is one of the magnetic eigenaxes. It has thus been chosen as the reference of the energies for the calculation of the MAE values:

$$\text{MAE} = E_{[uvw]} - E_{[010]}. \quad (11)$$

$E_{[uvw]}$  is the energy deduced from the spin-orbit calculations with magnetization along the  $[uvw]$  crystallographic direction. All our results have been crosschecked using the GGA+U calculations within the VASP code. It leads to exactly the same MAE values as the ones deduced from the WIEN2k collinear calculations. We have also realized noncollinear magnetic calculations in VASP which confirm the so-obtained magnetic eigenaxes. Thus, we have generated an antiferromagnetic order noted AF<sub>1</sub> shown in Fig. 8(a) respecting these conditions, which has been used to estimate the MAE of  $\text{SeCuO}_3$  with the WIEN2k code.

SOC is included as a perturbation of the antiferromagnetic collinear state, leading to an energy lowering given by

$$\Delta E_{\text{SOC}} = \frac{|\langle i | \widehat{H}_{\text{SOC}} | j \rangle|^2}{|\varepsilon_i - \varepsilon_j|}, \quad (12)$$

which accounts for an interaction between an occupied state  $i$  with an energy  $\varepsilon_i$  and an unoccupied state  $j$  with an energy  $\varepsilon_j$  via the matrix element  $\langle i | \widehat{H}_{\text{SOC}} | j \rangle$ . The resulting MAE is represented in Fig. 9(b), showing a uniaxial anisotropy along the  $b$  direction, while the hard axis is in the  $ac$  plane. A similar result is observed considering the on-site PBE0 hybrid functional. To be more quantitative, Table I gathers the MAE values for the magnetic eigenaxes of the AFM state (below  $T = 6$  K), deduced from torque measurements and highlighted in Fig. 3. The MAE values are expressed relatively to the MAE in the  $[010]$  crystal direction.

First of all, we have tested two different functionals, i.e., GGA+U and the on-site PBE0 hybrid. It appears that GGA+U with  $U_{\text{eff}} = 5$  eV leads to MAE values similar to the ones obtained with PBE0. The difference between the easy axis (along  $b$ ) and the two other directions is about  $10 \mu\text{eV}/\text{f.u.}$  If we consider a larger correction ( $U_{\text{eff}} = 9$  eV),

TABLE I. MAE values ( $\mu\text{eV}/\text{f.u.}$ ) for the magnetic eigenaxes of the AFM state, obtained with PBE0, GGA+U with  $U_{\text{eff}} = 9$  and 5 eV (noted 9 and 5, respectively), or by substituting zinc for copper (noted Zn). Directions  $[\bar{1} 0 1]^*$  and  $[1 0 1]$  represent easy and intermediate axes obtained from experiment. MAE values are given considering the  $[010]$  magnetization direction as the reference of the energies.

$U_{\text{eff}}^{\text{Cu1}}/U_{\text{eff}}^{\text{Cu2}}$	$[1 0 1]$	$[\bar{1} 0 1]^*$
9/9	4	5
9/Zn	-2	-1
Zn/9	5	9
5/5	9	9
5/Zn	-4	-2
Zn/5	11	19
PBE0/PBE0	11	14

as in Ref. [31] for  $\text{SrCu}_2(\text{BO}_3)_2$ , the MAE values are reduced by a factor of two, but the trend is conserved; i.e.,  $b$  is still predicted to be the easy axis in disagreement with the experimental facts. To understand this discrepancy, we first consider the Bruno relation [32]. According to this model, which is based on the SOC perturbation expression of Eq. (12) and ignoring spin-flip terms, the MAE is directly proportional to the orbital moment anisotropy

$$\text{MAE} = E_{\text{hard}} - E_{\text{easy}} = \frac{\xi}{4} |\langle L_z \rangle_{\text{hard}} - \langle L_z \rangle_{\text{easy}}|, \quad (13)$$

where  $\langle L_z \rangle$  is the orbital angular momentum. The  $\langle L_z \rangle$  term in Eq. (13) is shown in Fig. 8(b) for the four copper sites of one tetramer. For clarity, arrows highlight the direction for which the orbital momentum is maximum, pointing along the normal of each  $\text{CuO}_4$  plaquette. Summing the orbital moment of all copper sites leads to a total orbital moment which is maximal along the  $b$  direction. Thus, arguments based on both orbital moments and total energy lead to the same conclusion, i.e., an easy axis along the  $b$  direction, in contradiction to the experimental data. It should be noticed that as expected for a spin- $\frac{1}{2}$  system, the dipolar contribution is negligible, less than  $0.7 \mu\text{eV}/\text{f.u.}$

In addition, the present DFT calculations cannot reproduce another experimental fact which is the different magnetic moments at Cu1 and Cu2 sites,  $0.46$  and  $0.73 \mu_B$ , respectively, from NPD [12]. Indeed, DFT gives similar magnetic moments for Cu1 and Cu2, i.e.,  $0.84$  and  $0.75 \mu_B$  considering  $U_{\text{eff}} = 9$  and 5 eV, respectively. While  $U_{\text{eff}} = 5$  eV allows us to properly describe the magnetic moment of Cu2, it cannot explain the reduced value obtained from experiment for Cu1. Such a feature appears to be related to the fact that, as in  $\text{CdCu}_2(\text{BO}_3)_2$ , Cu1 ions form strongly coupled singlets, which are polarized by the staggered field of Cu2 spins, and Cu1 and Cu2 magnetic subsystems are decoupled.

We have then estimated the contribution of each inequivalent copper site to the MAE. MAE of Cu1 sites (noted MAE1) was calculated by substituting zinc for copper on all Cu2 sites, and MAE of Cu2 sites (noted MAE2) reversely [33]. Indeed,  $\text{Zn}^{2+}$  and  $\text{Cu}^{2+}$  cations share nearly the same radii,  $0.74$  and  $0.71 \text{ \AA}$ , respectively. In addition,  $\text{Zn}^{2+}$  is nonmagnetic ( $d^{10}$  electronic configuration) allowing the suppression of the magnetic response of Zn-substituted sites. A representation

of these partial MAEs is given in Fig. 9(b). In particular, the easy magnetization axis is located in the  $ac$  plane and along the  $b$  direction for MAE1 and MAE2, respectively. However, MAE2 is larger in amplitude than MAE1, leading to a total contribution to MAE dictated by MAE2, i.e., an easy axis along the  $b$ .

Our calculations demonstrate the predominant role of the Cu2 subsystem in the magnetic anisotropy of  $\text{SeCuO}_3$ , but remain incomplete because we do not reproduce the magnetic moment reduction of Cu1. As already mentioned above, such a feature is a consequence of (1) the formation of Cu1 dimers which are in a singlet state at low temperature ( $T < 200 \text{ K}$ ), (2) the spin fluctuations of Cu1 spins which are different from the ones of Cu2, leading to the decoupling of the two subsystems, and (3) the staggered field of the Cu2 subsystem which polarizes the magnetic moments of Cu1, leading to a strong decrease of its value [34].

From our point of view, all these experimental data converge to one model for  $\text{SeCuO}_3$ , consisting of nearly isolated Cu1 dimers immersed in the staggered field of the AFM long-range order of the Cu2 subsystem. One simple approach is to reduce the Hubbard correction on the Cu1 site, and indeed this leads to decrease of Cu1 magnetic moments from  $0.84$  to  $0.75$  and  $0.60 \mu_B$ , with  $U_{\text{eff}} = 9, 5,$  and  $0$  eV, respectively. Reducing  $U_{\text{eff}}$  even more to negative values will lead to entering an attractive electron-electron interaction regime. Such an attractive Hubbard model has been previously used as an effective description for systems involving strong electron-phonon coupling [35]. Indeed, strong spin-lattice coupling in the low-temperature state of  $\text{SeCuO}_3$  has been proposed by Lee *et al.*, based on the measurement of the nuclear spin-lattice relaxation rate  $1/T_1$  [11].

Here the idea is to simulate an extreme situation for which the electron-phonon coupling involving the Cu1 dimers would be enough to overcome the electron-electron Coulomb repulsion. It will correspond to the observation of attractive and repulsive regimes at low and high energy scales, respectively [35]. Interestingly, calculating the MAE with two sizable different treatments for Cu1 and Cu2 subsystems reproduces the experimental observation. More specifically, we have used  $U_{\text{eff}} = 0$  eV for Cu1 and  $U_{\text{eff}} = 5$  eV for Cu2. This choice allows us to reproduce, in an effective manner, the magnetic moment of Cu2 and the reduction of magnetic moments of Cu1. Such treatment leads to a 3D shape shown in Fig. 10(b), for which the  $b$  direction is properly found as being the hard axis and the easy axis lying in the  $ac$  plane. To be more quantitative, we compare in Table II the MAE values for the magnetic eigenaxes of the AFM state with respect to the  $b$  axis. It now appears that, among these three directions,  $[0 1 0]$  is systematically the hard one, and  $[1 0 1]$  the easy one. In other words, by considering that Cu1 and Cu2 subsystems are decoupled and by taking into account the reduction of the magnetic moment of Cu1, we are able to reproduce the experimental hard magnetization axis along the  $b$  direction. The easy axis is found to be in the  $ac$  plane in agreement with experimental refinements, but still not in the  $[\bar{1}01]^*$  direction (see Fig. 10).

At this stage, it should be mentioned that Bousquet *et al.* [36] have demonstrated that defining explicitly the exchange-correction parameter  $J$ , in the LSDA/U treatment,

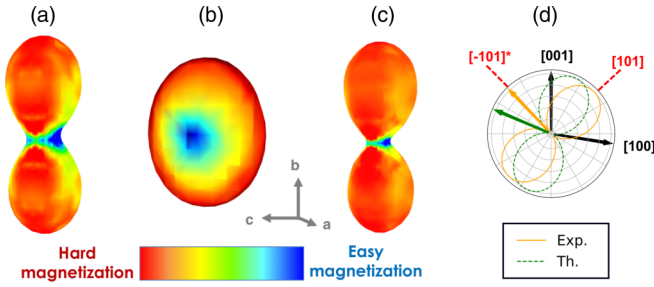


FIG. 10. (a) Experimental MAE. (b) MAE considering  $U_{\text{eff}} = 0$  eV for Cu1 and  $U_{\text{eff}} = 5$  eV for Cu2. (c) Similar to previous, except a  $U = 5$  eV and  $J = 0.5$  eV correction on Cu2. (d) A detailed comparison between the experimental MAE (solid lines) and theoretical MAE shown in (c) (dotted lines) in the  $ac$  plane.

strongly affects the noncollinear magnetic ground state, and more specifically the spin canting and the magnetocrystalline anisotropy shape. This constitutes a really delicate issue because it implies an adjustment of the amplitude of two parameters,  $U$  and  $J$ . Our results for  $U = 5$  eV and  $J = 0.5$  eV are summarized in Table II. It should be noticed that a similar trend of values is obtained using  $J = 1$  eV, confirming that the more important aspect is to explicitly specify the  $J$  value. Interestingly, the experimental MAE eigenaxes are properly described as soon as  $J$  is explicitly defined [see Fig. 10(c)]. More specifically, when both Cu1 and Cu2 are corrected, MAE values are 0,  $-7$ , and  $-20$   $\mu\text{eV}/\text{f.u.}$  for the  $[0\ 1\ 0]$ ,  $[1\ 0\ 1]$ , and  $[\bar{1}\ 0\ 1]^*$  directions, respectively. When the correction is added only on Cu2, the MAE values are 0,  $-26$ , and  $-32$   $\mu\text{eV}/\text{f.u.}$  for the identical respective directions. Such results demonstrate a drastic change of the MAE, mainly on the intermediate eigenaxes. In such a case, both explicit  $J$  definition on Cu2 and reduced Hubbard correction on Cu1 are necessary to properly orientate the theoretical easy axis along the experimental one, as represented in Fig. 10(c). In order to verify how the MAE2 behaves with such treatment, we redo a chemical substitution by Zn atoms on Cu1 sites. As expected, the MAE is strongly modified with respect to the one determined using an  $U_{\text{eff}}$  treatment [Fig. 10(b)], i.e., with easy, intermediate, and hard axes in good agreement with the experimental ones, as can be witnessed from Figs. 10(a) and 10(c). Figure 10(d) shows that the deviation in the  $ac$  plane between the experimental and theoretical MAE is reduced to  $24^\circ$ . To summarize, the hard axis is well predicted to be along the  $b$  axis and the easy and intermediate axes are found to be in the  $ac$  plane. We still have a sizable deviation which is

TABLE II. MAE values ( $\mu\text{eV}/\text{f.u.}$ ) for the magnetic eigenaxes of the AFM state obtained with different GGA+U treatments for copper atoms. We report values obtained for (i)  $U_{\text{eff}} = 5$  eV, and  $U = 5$  eV and  $J = 0.5$  eV. MAE values are given considering the  $[010]$  magnetization direction as the reference of the energies.

Cu1	$U_{\text{eff}} = 5$	$U_{\text{eff}} = 0$	$U = 5, J = 0.5$	$U_{\text{eff}} = 0$
Cu2	$U_{\text{eff}} = 5$	$U_{\text{eff}} = 5$	$U = 5, J = 0.5$	$U = 5, J = 0.5$
$[1\ 0\ 1]$	9	-10	-7	-26
$[\bar{1}\ 0\ 1]^*$	9	-7	-20	-32

expected because of the mean-field treatment which has been used to simulate the MAE. It should be noticed that the overall shape of the MAE was unchanged when considering  $J = 0.5$  and 1 eV for  $U = 5$  eV.

#### IV. DISCUSSION

Torque magnetometry is a convenient method for studying magnetocrystalline anisotropy and spin reorientation phenomena in a finite magnetic field since the angular dependence of torque is very sensitive to the orientation of the spin axis in magnetically ordered materials. In this work we combine torque magnetometry with a simple phenomenological approach to magnetic anisotropy in order to probe the spin reorientation in low-dimensional antiferromagnet  $\text{SeCuO}_3$ . Our analysis shows that under the assumption of spin reorientation in a collinear antiferromagnet we are able to reproduce qualitatively the shape of the torque curves in  $\text{SeCuO}_3$  (dotted lines in Fig. 5). However, the obtained independence of torque amplitude from magnetic field for  $H \geq H_{\text{SF}}$ , which is also found for other collinear antiferromagnets [26,28], is not observed in  $\text{SeCuO}_3$  [see Fig. 2(b) and Fig. 5]. Contrary to expectations and our simple model, torque amplitude increases linearly with  $H^2$  for  $H \geq H_{\text{SF}}$  but with a much smaller slope than for  $H \ll H_{\text{SF}}$  [Fig. 2(b)]. We further show that the experimental result is a consequence of the existence of two subsystems in  $\text{SeCuO}_3$ , where only one exhibits the spin reorientation in applied magnetic fields.

The existence of two subsystems in  $\text{SeCuO}_3$  was already proposed in Ref. [7] where it was suggested that the correlations between Cu1 and Cu2 in  $\text{SeCuO}_3$  are site-selective and strong coupling between Cu1 spins might form a singlet state at higher temperatures, thus separating Cu1 and Cu2 spin sublattices. The scenario of two subsystems made of the strongly coupled Cu1 dimers and the weakly coupled Cu2 spins in the AFM state was recently proposed from NMR measurements which witnessed different temperature evolution of  $1/T_2$  assigned to Cu1 and Cu2 spins in the AFM state [11]. The NQR measurements showed that Cu1 dimers indeed form singlets already at high temperatures  $T < 200$  K, while Cu2 spins are only weakly coupled to the central pair [12]. The significantly reduced value of magnetic moment of Cu1 compared to Cu2 [12] corroborates this picture.

The proposed two-subsystem scenario for  $\text{SeCuO}_3$  is very similar to the case of the ordered AFM state in  $\text{CdCu}_2(\text{BO}_3)_2$  in which spins  $S_a$  and  $S_d$  are related to the Cu2 site, while  $S_b$  and  $S_c$  to the Cu1 site. In this system, the spins of Cu1 atoms form strongly coupled singlets, but at  $T_N \leq 9.8$  K, antiferromagnetic long-range order sets in due to much weaker intertetramer interactions. Neutron powder diffraction (NPD) measurements on this system reported a smaller magnetic moment on the Cu1 than on the Cu2 site [37]. A theoretical investigation of  $\text{CdCu}_2(\text{BO}_3)_2$  showed dominant coupling between Cu1 spins forming AFM dimers, while weaker intratetramer and intertetramer interactions are responsible for the low-temperature AFM long-range ordering of Cu2 spins [34]. The same study revealed that the polarization of Cu1 singlets is possible because the field from Cu2 spins is staggered and thus does not commute with the exchange interaction on the dimer [34]. Janson *et al.* further showed that a significant

magnetic moment can be induced on Cu1 spins by the staggered field from Cu2 spins [34]. This picture, later confirmed experimentally by NMR and ZF- $\mu$ SR measurements [6], is different from the usual long-range order which is induced by the interactions between the spins. In  $\text{CdCu}_2(\text{BO}_3)_2$  the magnetic interactions are responsible for the magnetic order of the Cu2 site only, while Cu1 moments are polarized. The decoupling of the Cu1 and Cu2 spins in the ordered state is witnessed by a magnetic anomaly at  $T^* = 6.5$  K observed in NMR, which was attributed to the reorientation of Cu2 spins, while Cu1 remains intact [6]. Based on the results published on  $\text{SeCuO}_3$  so far, it seems that one can draw a parallel between these two systems.

The two decoupled subsystems in  $\text{SeCuO}_3$  that we propose from our results correspond to Cu1 and Cu2 spins, respectively. Since half of the spins in  $\text{SeCuO}_3$  are Cu1 spins and the other half are Cu2 spins, we can now write for the susceptibility of Cu1  $\chi_1 = n \chi_0 = m \cdot (0.5 \cdot \chi_0)$ . The contribution of Cu1 spins to the total  $\chi_0$  is reduced by  $m$  due to the decoupling of the two sublattices. For  $n = 0.22$  obtained in Sec. III B we get  $m = 0.44$ . The induced magnetization on Cu1 spins is only 44% of the value it would be if these spins were equivalent to Cu2 spins. It is tempting to compare this to the ratio of magnetic moments  $m_{\text{Cu1}}/m_{\text{Cu2}} \approx 0.35/0.8 = 0.44$  obtained for magnetic moments on Cu1 and Cu2 from neutron data [12]. However, this comparison may not be justified if Cu1 and Cu2 belong to decoupled subsystems. The ratio  $\chi_1/\chi_2 = n/(1-n) = 0.282$  confirms that the magnetization induced on Cu2 spins is significantly larger than on Cu1 spins. This picture corroborates that the dominant contribution to the total MAE comes from the Cu2 site.

Having now established arguments for two decoupled subsystems we can construct a more rigorous model of the magnetic structure and spin reorientation in  $\text{SeCuO}_3$  by including also the symmetry arguments. Our proposal of zero-field and spin-flopped magnetic structures in  $\text{SeCuO}_3$  is shown in Fig. 11. The previously published susceptibility anisotropy in the AFM state strongly supports a picture of collinear or very weakly canted AFM state in zero magnetic field [7,10] which is why we propose the collinear zero-field structure plotted in Figs. 11(a) and 11(c) for the AFM state of  $\text{SeCuO}_3$ . Our theoretical investigations based on a similar magnetic ordering do not allow us to obtain a better picture of this magnetic ordering with respect to the crystal axes. To propose a specific orientation of the spins shown in Figs. 11(a) and 11(c), we rely on symmetry elements as well as results from the literature which allow us to assume AFM coupling between Cu1 spins [12] and AFM coupling between Cu1 and Cu2 spins on the tetramer [7]. In zero field all spins are oriented along the  $(\bar{1} 0 1)^*$  direction (Ref. [10] and this work). Both Cu1 and Cu2 moments are confined to their respective  $\text{CuO}_4$  plaquettes. Our result is in agreement with the recently published NPD data which state that Cu2 spins lie within the plaquette and NQR data which state that Cu1 spins lie within their plaquette [12]. Strongly noncollinear magnetic structure proposed by the same authors in their unpublished work [38] is in disagreement with our result as well as previously published magnetic susceptibility anisotropy [7,10] which only allows for collinear or very weakly canted spins, as we mentioned above. Indeed, the magnetic susceptibility

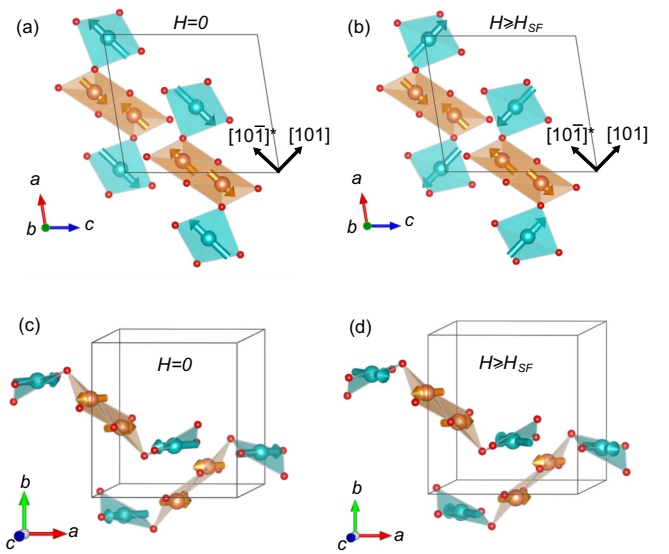


FIG. 11. The magnetic structure in AFM state in zero field (a) and (c) and in field  $H \geq H_{\text{SF}}$  applied along the easy axis (b) and (d) obtained in this work. (a) and (b) show the  $ac$  plane to which the spins are confined. In (a) and (b) the directions of the easy  $(\bar{1} 0 1)^*$  and intermediate  $[101]$  axes obtained from experiment are also shown.

measured along the easy axis in  $\text{SeCuO}_3$  goes practically to zero as  $T \rightarrow 0$  [7]. Such a feature will not be observed in strongly noncollinear magnetic structures. Furthermore, based on our results where only one subsystem reorients in finite magnetic field, we propose a structure shown in Figs. 11(b) and 11(d) in applied magnetic field  $H \geq H_{\text{SF}}$  where the spins on Cu1 remain in the zero-field orientation, while the Cu2 spins flop to the  $(101)$  direction.

In order to confirm the present picture, we have realized DFT+U+SOC calculations [14,39] using the VASP code [40–42] to take into account the potential noncollinearity. More specifically, we have used an energy cutoff of 550 eV, a similar  $k_{\text{mesh}}$  to the one in WIEN2k, and the convergence criterion was fixed at  $10^{-7}$  eV. Starting from a collinear antiferromagnetic arrangement with all the spins oriented along the  $(\bar{1} 0 1)^*$ , we obtained a small but significant noncollinearity between Cu1 and Cu2 spins, with a canting angle ranging from  $0.2^\circ$  to  $1^\circ$  depending on the  $U$  (from 5 to 7 eV) and  $J$  (from 0 to 1 eV) values. This last result confirms that  $\text{SeCuO}_3$  can be viewed as a slightly canted antiferromagnet, but the canting is too weak to produce an effect in our macroscopic measurements. It also justifies the WIEN2k calculations reported in the present paper, which have been done using a collinear antiferromagnetic model. These calculations have demonstrated that an explicit definition of the exchange-correlation term  $J$  in the GGA+U+SOC calculations is needed to properly describe the MAE eigenaxes. Moreover, by taking into account, in an effective manner, the different correlation regime of Cu1 and Cu2 subsystems, we are able to reproduce the reduction of the Cu1 magnetic moment and the relative amplitudes of MAE1 and MAE2.

A chemical interpretation of these results can be reached by examining the projected densities of states (PDOSs). Indeed, such analysis allows us to determine the most important

interactions, which are the ones with the smallest energy gap  $|\varepsilon_i - \varepsilon_j|$ , as defined in Eq. (12). More precisely, the observed spin orientations of such  $\text{Cu}^{2+}$   $S = \frac{1}{2}$  system can be interpreted by the inspection of the PDOS and thus the interactions involving the crystal-field split  $d$  states of each magnetic  $\text{Cu}^{2+}$  ion, under the action of the spin-orbit coupling. Figures 12(a) and 12(b) show the split of Cu1 and Cu2  $d$  states using GGA+U calculations, with  $U_{\text{eff}} = 5$  eV. It should be noted that the PDOSs obtained with and without specifying explicitly the exchange-correction term  $J$  are similar. Here, we defined the local coordinate system with  $x$  and  $y$  inside the  $\text{CuO}_4$  plane, pointing towards oxygen atoms, and  $z$  perpendicular to the  $\text{CuO}_4$  plaquette as shown in Fig. 12(a). The overall features for the PDOSs of Cu1 and Cu2 are the same, with an empty  $(x^2 - y^2)$  state. In such a situation, the  $\langle d_{xy} \downarrow | \hat{H}_{\text{SOC}} | d_{x^2-y^2} \downarrow \rangle$ ,  $\langle d_{xz} \downarrow | \hat{H}_{\text{SOC}} | d_{x^2-y^2} \downarrow \rangle$ , and  $\langle d_{yz} \downarrow | \hat{H}_{\text{SOC}} | d_{x^2-y^2} \downarrow \rangle$  interactions will be nonzero and mainly active because closer to the Fermi level. Spins with orientation inside the plaquette ( $\parallel xy$  spin orientation) will be favored if  $d_{xz} \downarrow$  or  $d_{yz} \downarrow$  states are closer to the empty  $d_{x^2-y^2} \downarrow$  states. In contrast, if  $d_{xy} \downarrow$  states are closer, spins with orientation perpendicular to the  $\text{CuO}_4$  plaquette ( $\perp xy$  spin orientation) will be favored. In the present case, the interpretation is not straightforward due to the significant distortion of Cu1 and Cu2 sites, which are far from regular  $\text{CuO}_4$  plaquettes. Only Cu1 PDOSs show relevant features, which can be interpreted. Indeed, the inset of Fig. 12(b) shows that the states which are mainly contributing on the top of the valence band are  $d_{xz}$  and  $d_{yz}$ , which leads to favoring the  $\parallel xy$  spin orientation, as witnessed in our DFT+U+SOC calculations when considering only the Cu1 subsystem, i.e., MAE1, which shows an easy magnetization axis in the  $ac$  plane. In contrast, the Cu2 PDOS does allow us to determine which  $d$  state is mainly contributing to the top of the valence band. Indeed, while such an analysis is relevant for systems exhibiting regular environments, it should be used with care for distorted environments, because the choice of the local axes for the PDOS is not anymore unique and may influence the results. Figure 12(c) shows the PDOS of Cu1 when considering no Hubbard correction ( $U_{\text{eff}} = 0$  eV). The main consequence is a significant band gap reduction and an increase of the  $d_{xz}$  and  $d_{yz}$  characters on the top of the valence band. Both modifications lead to an increase of the spin-orbit coupling which mixes the  $d_{xz}$  and  $d_{yz}$  occupied states with the  $d_{x^2-y^2}$  unoccupied state. Such treatment leads to having a larger contribution of MAE1 to the total MAE, which then develops an easy axis in the  $ac$  plane and hard axis along the  $b$  crystallographic direction.

To summarize, there is an agreement between the structure from Ref. [12] and our proposal shown in Figs. 11(a) and 11(c). Magnetic moments on Cu1 and Cu2 almost lie within their respective  $\text{CuO}_4$  plaquettes and our model also supports a much smaller magnetic moment on Cu1 than on Cu2. More detailed comparison with NPD is not possible since there were difficulties in interpreting the existing NPD and single-crystal data in Ref. [12]. Our results state that Cu1 moments should be collinear or almost collinear to Cu2 moments, in agreement with the susceptibility, magnetization, and torque data. Future investigation of magnetic structure by neutron diffraction on single crystals would resolve this issue.

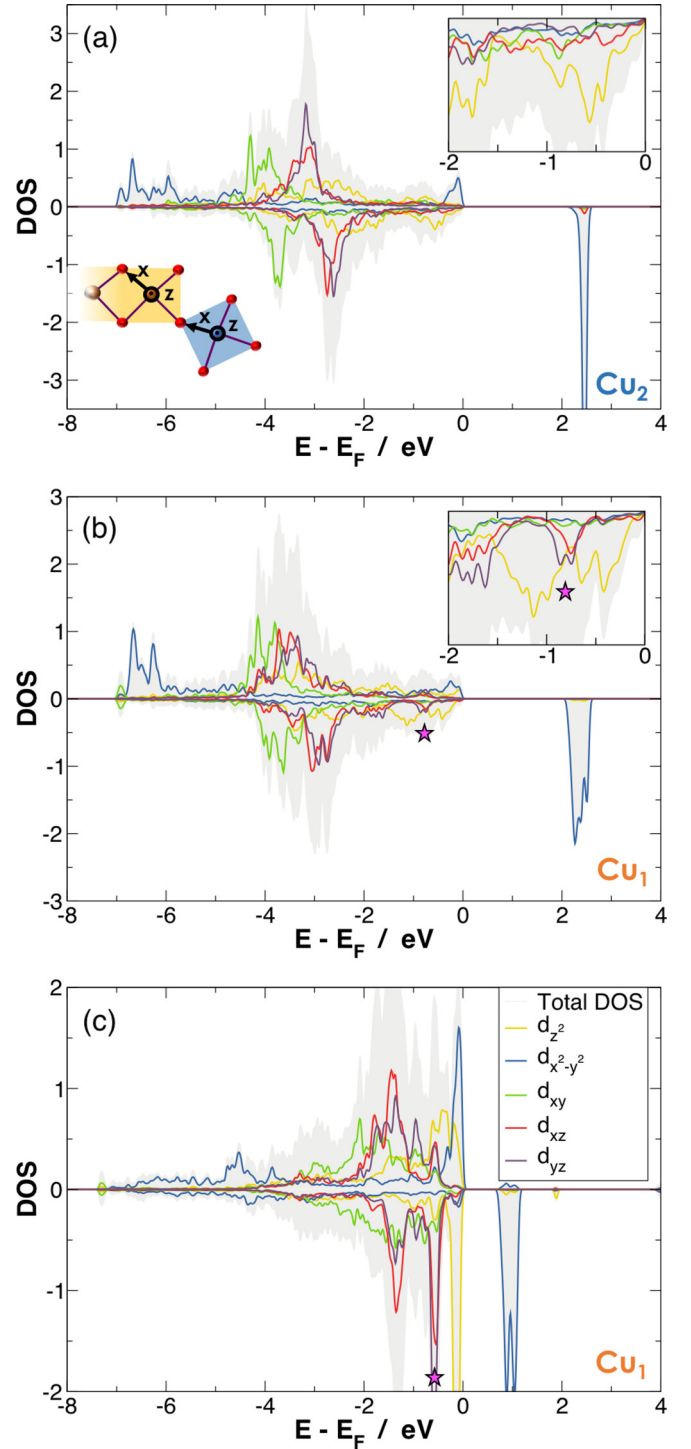


FIG. 12. Projected density of states (PDOS) on (a) Cu2 and (b) Cu1 sites considering a  $U_{\text{eff}} = 5$  eV, and on (c) Cu1 only at the GGA level. Projection axes for each Cu site are represented on the scheme in (a). Insets zoom in on the spin minority states over the range of 2 eV below the Fermi energy. Pink stars correspond to first excitations allowed with the excited states.

The decoupling of Cu1 and Cu2 subsystems is comparable to the observations in  $\text{Cu}_2\text{Cd}(\text{BO}_3)_2$  [6]. The question in  $\text{SeCuO}_3$  is, are the Cu1 spins polarized singlets in the underlying AFM state formed by interactions between Cu2

spins, or do both Cu1 and Cu2 spins interact mutually to form the AFM state? If Cu1 spins indeed form singlet states even in the AFM state then  $\chi_1$  and MAE1 should be much smaller than  $\chi_2$  and MAE2. In fact, if a true singlet state persists in the AFM state, for an intradimer interaction  $J \approx 200$  K between Cu1 spins we should expect  $\chi_1$  and MAE1 to be zero at low temperatures [43]. A finite slope of torque amplitude for the nonflopped spins (see Fig. 2) suggests Cu1 spins contribute with finite susceptibility anisotropy. Also,  $\chi_1/\chi_2 = 0.282$  obtained from our simulations is small but finite. From our data we cannot distinguish whether Cu1 spins in the AFM state form polarized singlets or contribute to the AFM order with a much smaller magnetic moment than Cu2 spins. The site-specific spin reorientation we observe favors the former picture, but further experiments are needed to confirm this.

If Cu1 spins are in fact polarized singlets we would have a similar scenario to  $\text{CdCu}_2(\text{BO}_3)_2$ . In this system neutron diffraction gave a sizable magnetic moment on Cu1 sites [37], while theoretical and experimental data showed that the Cu1-Cu1 dimer forms a singlet in the AFM state [6,34]. A similar scenario appears to apply to  $\text{SeCuO}_3$ , and indeed our DFT calculations which mimic the reduction of the Cu1 magnetic moment reproduce properly the experimental MAE. Magnetic order in  $\text{CdCu}_2(\text{BO}_3)_2$  is almost collinear with very small canting, similar to what we propose for  $\text{SeCuO}_3$ . One way to check our proposed magnetic structure in zero and finite field rigorously is to perform single-crystal neutron diffraction experiments in zero and finite applied magnetic field.

## V. CONCLUSION

The present paper proposes a combined experimental and theoretical investigation of the magnetic properties of a low-dimensional spin- $\frac{1}{2}$  system, which appears to be based on two decoupled magnetic subsystems. This finding, based on measurements on high-quality single crystals and

state-of-the-art density functional calculations, opens a way to very exciting physics, with the possibility to control separately two magnetic subsystems in one material.  $\text{SeCuO}_3$  was previously proposed as a candidate for a system with site-selective spin correlations where Cu1 copper atoms form strongly coupled AFM dimers, while the coupling including Cu2 spins results in a long-range AFM order at low temperatures. Our torque magnetometry results demonstrate site-specific spin reorientation in an applied magnetic field in the AFM state of  $\text{SeCuO}_3$ . Using an *ab initio* approach we show that Cu1 and Cu2 contribute differently to the magnetic anisotropy energy. These results strongly suggest that Cu1 and Cu2 spin systems are decoupled in  $\text{SeCuO}_3$ . Combining our experimental and theoretical findings we propose an antiferromagnetic structure of  $\text{SeCuO}_3$  in zero field, as well as in field  $H \gtrsim H_{\text{SF}}$ , to be verified by future experiments on this system.

## ACKNOWLEDGMENTS

M.H., N.N., Ž.R., and M.D. acknowledge full support of their work (torque experiment and simulation of torque data) by the Croatian Science Foundation under Grant No. UIP-2014-09-9775. M.H., M.D., W.L.-d.-H., and X.R. acknowledge support by COGITO project “Theoretical and experimental investigations of magnetic and multiferroic materials” funded by the Croatian Ministry of Science and Education and the French Agency for the Promotion of Higher Education, International Student Services, and International Mobility. W.L.-d.-H. and X.R. thank the CCIPL (Centre de Calcul Intensif des Pays de la Loire) for computing facilities. The theoretical work was also performed using HPC resources from GENCI-[TGCC/CINES/IDRIS] (Grant No. 2017-A0010907682). Crystal and magnetic structures in this work were drawn using the 3D visualization program VESTA [44].

N.N. and W.L.-d.-H. contributed equally to this work.

- 
- [1] A. Vasiliev, O. Volkova, E. Zvereva, and M. Markina, *npj Quantum Mater.* **3**, 2397 (2018).
  - [2] B. Sriram Shastry and B. Sutherland, *Physica B+C* **108**, 1069 (1981).
  - [3] M. E. Zayed, C. Rüegg, J. Larrea J., A. M. Läuchli, C. Panagopoulos, S. S. Saxena, M. Ellerby, D. F. McMorrow, T. Strässle, S. Klotz, G. Hamel, R. A. Sadykov, V. Pomjakushin, M. Boehm, M. Jiménez-Ruiz, A. Schneidewind, E. Pomjakushina, M. Stingaciu, K. Conder, and H. M. Rønnow, *Nat. Phys.* **13**, 962 (2017).
  - [4] J. T. Haraldsen, T. Barnes, and J. L. Musfeldt, *Phys. Rev. B* **71**, 064403 (2005).
  - [5] M. Hase, M. Kohno, H. Kitazawa, O. Suzuki, K. Ozawa, G. Kido, M. Imai, and X. Hu, *Phys. Rev. B* **72**, 172412 (2005).
  - [6] W.-J. Lee, S.-H. Do, S. Yoon, Z. H. Jang, B. J. Suh, J. H. Lee, A. P. Reyes, P. L. Kuhns, H. Luetkens, and K.-Y. Choi, *Phys. Rev. B* **90**, 214416 (2014).
  - [7] I. Živković, D. M. Djokić, M. Herak, D. Pajić, K. Prša, P. Pattison, D. Dominko, Z. Micković, D. Cinčić, L. Forró, H. Berger, and H. M. Rønnow, *Phys. Rev. B* **86**, 054405 (2012).
  - [8] H. Effenberger, *Z. Kristallogr.* **175**, 61 (1986).
  - [9] E. Shuji, T. Tadashi, and M. Yoneichiro, *Bull. Chem. Soc. Jpn.* **48**, 1649 (1975).
  - [10] M. Herak, A. Grubišić Čabo, D. Žilić, B. Rakvin, K. Salamon, O. Milat, and H. Berger, *Phys. Rev. B* **89**, 184411 (2014).
  - [11] S. Lee, W.-J. Lee, J. van Tol, P. L. Kuhns, A. P. Reyes, H. Berger, and K.-Y. Choi, *Phys. Rev. B* **95**, 054405 (2017).
  - [12] T. Cvitanić, V. Šurija, K. Prša, O. Zaharko, I. Kupčić, P. Babkevich, M. Frontzek, M. Požek, H. Berger, A. Magrez, H. M. Rønnow, M. S. Grbić, and I. Živković, *Phys. Rev. B* **98**, 054409 (2018).
  - [13] P. Blaha, K. Schwarz, G. K. H. Madsen, D. Kvasnicka, J. Luitz, R. Laskowski, F. Tran, and L. D. Marks, *WIEN2k, An Augmented Plane Wave + Local Orbitals Program for Calculating Crystal Properties* (Karlheinz Schwarz, Techn. Universität Wien, Austria, 2018).
  - [14] J. P. Perdew, K. Burke, and M. Ernzerhof, *Phys. Rev. Lett.* **77**, 3865 (1996).

- [15] V. I. Anisimov, I. V. Solovyev, M. A. Korotin, M. T. Czyzyk, and G. A. Sawatzky, *Phys. Rev. B* **48**, 16929 (1993).
- [16] F. Tran, P. Blaha, K. Schwarz, and P. Novák, *Phys. Rev. B* **74**, 155108 (2006).
- [17] H. J. Monkhorst, *Phys. Rev. B* **13**, 5188 (1976).
- [18] L. Néel, *Ann. Phys.* **11**, 232 (1936).
- [19] L. Néel, *Proc. Phys. Soc., Sect. A* **65**, 869 (1952).
- [20] H. Rohrer and H. Thomas, *J. Appl. Phys.* **40**, 1025 (1969).
- [21] A. N. Bogdanov, A. V. Zhuravlev, and U. K. Röbler, *Phys. Rev. B* **75**, 094425 (2007).
- [22] M. Herak, D. Žilić, D. Matković Čalogović, and H. Berger, *Phys. Rev. B* **91**, 174436 (2015).
- [23] M. Herak, M. Miljak, G. Dhalenne, and A. Revcolevschi, *J. Phys.: Condens. Matter* **22**, 026006 (2010).
- [24] M. Herak, *Solid State Commun.* **151**, 1588 (2011).
- [25] For a monoclinic system Neumann's principle dictates that the  $b$  axis must be one of the magnetic eigenaxes,  $m_2 = b$ , while the other two eigenaxes,  $m_1$  and  $m_3$ , can have any orientation in the  $ac$  plane [27]. In coordinate system spanned by axes  $(m_1, m_2 = b, m_3)$  magnetocrystalline anisotropy energy for a monoclinic system is usually written as  $\mathcal{F}_a(\theta, \phi) = K_0 + K_1 \cos^2 \theta + K_2 \sin^2 \theta \cos 2\phi$ . Writing the MAE in a coordinate system where we chose  $m_3 = b$  as in the text leads to Eq. (5).
- [26] H. Uozaki, T. Sasaki, S. Endo, and N. Toyota, *J. Phys. Soc. Jpn.* **69**, 2759 (2000).
- [27] R. E. Newnham, *Properties of Materials (Anisotropy, Symmetry, Structure)* (Oxford University Press, New York, 2005).
- [28] M. Tokumoto, H. Tanaka, T. Otsuka, H. Kobayashi, and A. Kobayashi, *Polyhedron* **24**, 2793 (2005).
- [29] Absolute values of anisotropy constants obtained from our simulations have some small uncertainty, but the difference  $K_1 - K_2$  must always be such to reproduce the values of the spin-flop field.
- [30] X. Rocquefelte, K. Schwarz, P. Blaha, S. Kumar, and J. van den Brink, *Nat. Commun.* **4**, 2511 (2013).
- [31] G. Radtke, A. Saúl, H. A. Dabkowska, M. B. Salamon, and M. Jaime, *Proc. Natl. Acad. Sci. USA* **112**, 1971 (2015).
- [32] P. Bruno, *Phys. Rev. B* **39**, 865 (1989).
- [33] C. Weingart, N. Spaldin, and E. Bousquet, *Phys. Rev. B* **86**, 094413 (2012).
- [34] O. Janson, I. Rousochatzakis, A. A. Tsirlin, J. Richter, Y. Skourski, and H. Rosner, *Phys. Rev. B* **85**, 064404 (2012).
- [35] R. Žitko, Ž. Osolin, and P. Jeglič, *Phys. Rev. B* **91**, 155111 (2015).
- [36] E. Bousquet and N. Spaldin, *Phys. Rev. B* **82**, 220402 (2010).
- [37] M. Hase, A. Dönni, V. Y. Pomjakushin, L. Keller, F. Gozzo, A. Cervellino, and M. Kohno, *Phys. Rev. B* **80**, 104405 (2009).
- [38] T. Cvitanić, V. Šurija, K. Prša, O. Zaharko, P. Babkevich, M. Frontzek, M. Požek, H. Berger, A. Magrez, H. M. Rønnow, M. S. Grbić, and I. Živković, [arXiv:1801.01431](https://arxiv.org/abs/1801.01431).
- [39] A. I. Liechtenstein, V. I. Anisimov, and J. Zaanen, *Phys. Rev. B* **52**, R5467(R) (1995).
- [40] G. Kresse and J. Furthmüller, *Phys. Rev. B* **54**, 11169 (1996).
- [41] G. Kresse and J. Furthmüller, *Comput. Mater. Sci.* **6**, 15 (1996).
- [42] G. Kresse and D. Joubert, *Phys. Rev. B* **59**, 1758 (1999).
- [43] B. Bleaney and K. D. Bowers, *Proc. R. Soc. London A* **214**, 451 (1952).
- [44] K. Momma and F. Izumi, *J. Appl. Crystallogr.* **44**, 1272 (2011).